Electronic Supplementary Material (ESI) for Lab on a Chip.

Deformation under flow and morphological recovery of cancer cells †

Emile Gasser[a,b], Emilie Su[b,c], Kotryna Vaidziulytė[d], Nassiba Abbade[a,d], Hamiza Cognart[a], Jean-Baptiste Manneville[c], Jean-Louis Viovy[a], Matthieu Piel[d], Jean-Yves Pierga[e], Kyohei Terao*[f], and Catherine Villard*[b]‡

[a] Université PSL, Institut Curie and Institut Pierre Gilles de Gennes, Physico-Chimie Curie, CNRS UMR168, F-75005 Paris, France.
[b] Université Paris Cité, Laboratoire Interdisciplinaire des Energies de Demain, CNRS UMR 8236, F-75013, Paris, France.
[c] Université Paris Cité, Laboratoire Matière et Systèmes Complexes (MSC), CNRS UMR 7057, 10 rue Alice Domon et Léonie Duquet, F-75013 Paris, France.
[d] Université PSL, Institut Curie and Institut Pierre Gilles de Gennes, CNRS UMR144, F-75005 Paris, France.
[e] Département d'Oncologie Médicale de l'Institut Curie et Université Paris Cité.
[f] Kagawa University, Nano-Micro Structure Device Integrated Research Center, 2217-20 Hayashi-cho, Takamatsu 761-0396, Japan.

Supplementary information

1 - Effective radius of the constrictions

The equations used to derive rheological parameters[1] have been established in the case of a cylindrical pipette of radius R. To be applied to the rectangular constriction of the Pachinko microfluidic device, R needs to be replaced with an effective radius R_{eff} that is a function of the constriction width w and height h. Referring to the theory for rectangular channels established in[2], the expression for R_{eff} is given by:

$$R_{eff}^4 = \frac{2}{\pi} \frac{w \times h^3}{(1+h/w)^2 \times g^*(h/w)} \tag{1}$$

with g^* a dimensionless function of the form

$$g^*(x) = \left[\left(1+\frac{1}{x}\right)^2 \left(1 - \frac{192}{\pi^5 x} \sum_{i=1,3,5}^{\infty} \frac{\tanh\left(\frac{\pi}{2} i x\right)}{i^5}\right)\right]^{-1} \tag{2}$$

With $w = 6\mu$m the width and $h = 15\mu$m the height of the rectangular channel, applying Eq.1 and Eq.2 yields $R_{eff} = 6.27\mu$m.

2 - Profile of the constrictions

Upon fabrication of the wafer molds, the height of structures were checked using a mechanical profilometer (dektak 6M, Veeco). We also used an optical profilometer (NT9100, Veeco) to obtain 3D imaging of constrictions (Fig. S1a-b). Diffraction during exposure limits the achievable resolution of structures obtained with photolithography. The actual width of the constriction ranges from ≈ 5µm at the top to ≈ 7 µm at the bottom of the structure. We consider this distribution to be acceptable, and will refer to the constriction as a rectangle of 6 µm width. These results were confirmed by the observation of the structures in the PDMS chip by scanning electron microscopy.

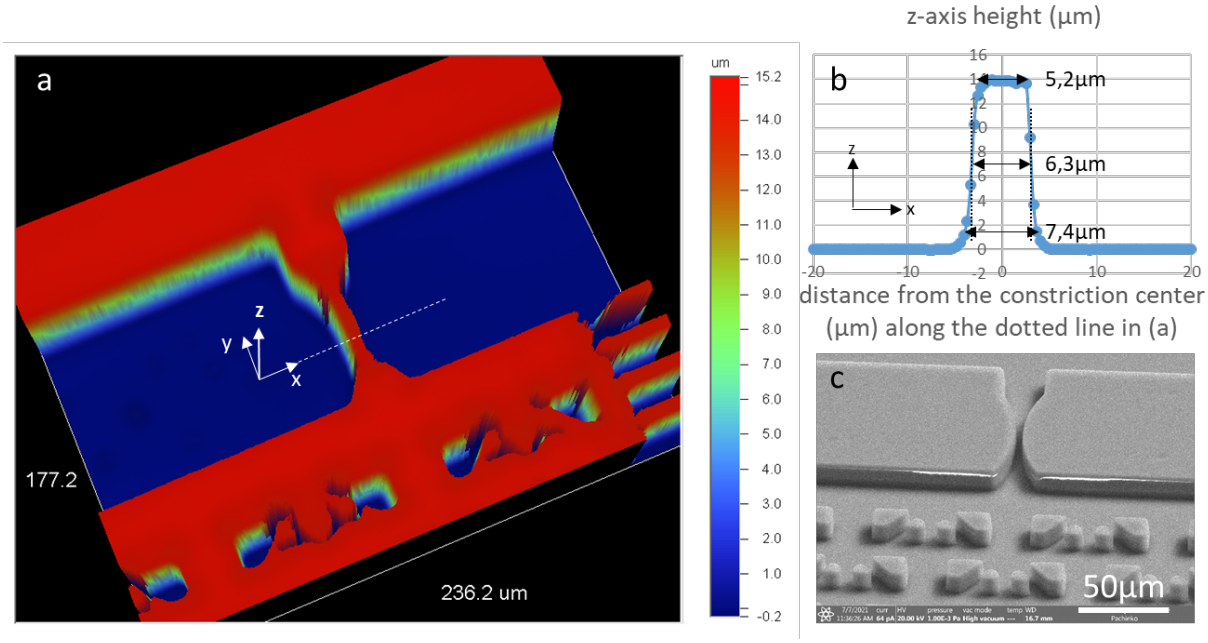

Figure S1 - Detail of a constriction a) 3D visualisation of a constriction height measured on the wafer used to produce the microfluidic chips, using an optical profilometer (NT9100, Veeco). b) Detail of the profile of the cross-section of a constriction at its narrowest point. Due to photolithography limitations, constriction width ranges from 7µm at the base to 5µm at the top. Thus for simplification, the constriction was considered as a rectangle of 6µm width. c) Scanning Electron Microscopy view of the constriction and single cell nests trap chamber, taken on a PDMS chip before bonding to the fluorodish.

3 - Numerical simulations

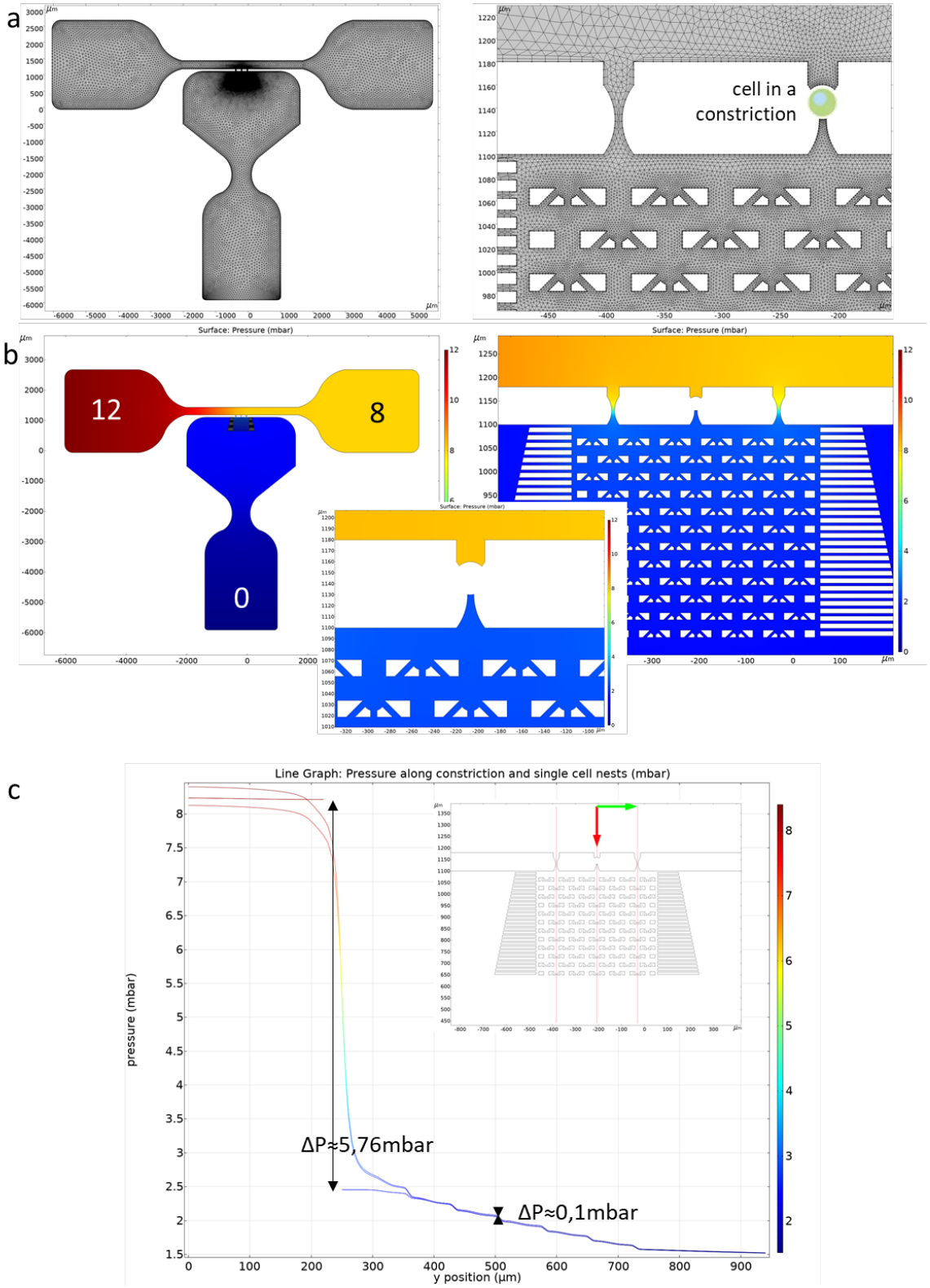

Figure S2 - Numerical simulations performed on the Pachinko device. a) Representation of the mesh used for finite elements calculations. Meshing was refined close to the constriction and single cell nests (minimal element size was set to 0.172 µm). b) Representation of the pressure profile within the device. Inlet 1, outlets 2 and 3 pressure were set respectively to 12, 8 and 0 mbar. Most of the pressure drop is located on the constrictions. The shallow channel approximation was used to take into account the effect of the channel height on the pressure profile. c) The middle constriction was closed to mimic the effect of a cell within a constriction. The resulting pressure differences applied between the front and back of the cell is approximately $\Delta P_h \approx$5.76 mbar. Residual pressure drop located in the single cell nests is ≈0.1 mbar, and thus can be neglected in front of the pressure drop applied within the constriction.

Table S2 - Pressure Differences ΔP as a function of the possible configurations of constrictions occupancy by cells. Values are obtained through numerical simulations with Comsol (see Fig.S2). The plot for the configuration "1 cell in the middle constriction" is represented on Fig.S2c. Experimentally we observed that in average only one constriction was used at the same time, for calculations purposes we'll then use $\Delta P = 6 \pm 0.25$ mbar.

ΔP in constriction / Nb cells in constrictions	Left	Middle	Right
1 cell	6.19mbar	open	open
	open	5.76mbar	open
	open	open	5.86mbar
2 cells	open	7.35mbar	7.46mbar
	7.50mbar	open	7.22mbar
	7.80mbar	7.40mbar	open
3 cells	10.15mbar	10.0mbar	9.88mbar

4 - Membrane curvature-induced pressure differences

As the cell membrane is being curved in the constriction, a pressure difference ΔP_c is created which opposes cell deformation and counteracts the hydrostatic pressure difference ΔP_h. Laplace law defines the relation between the inside and outside pressures around a curved membrane as:

$$\Delta P = P_{inside} - P_{outside} = \tau_0 \left(\frac{1}{R_1} + \frac{1}{R_2} \right)$$

where τ_0 is the membrane tension, and R_1 and R_2 are the principal curvature radii. We apply this relation at the back and front of the cell:

$$\Delta P^{back} = P_{inside} - P^{back}_{outside} = \tau_0 \left(\frac{1}{R_{back}} + \frac{1}{R_h} \right) \text{ and } \Delta P^{front} = P_{inside} - P^{front}_{outside} = \tau_0 \left(\frac{1}{R_{front}} + \frac{1}{R_h} \right)$$

where R_{back} and R_{front} are the radii of the back and front radii of the cell in an horizontal plane, and R_h the inverse of the vertical curvature defined between the floor and ceiling of the microchannel of height h. We define the resulting pressure difference created by the membrane curvatures ΔP_c as[3,4]:

$$\Delta P_c = P^{back}_{outside} - P^{front}_{outside} = \tau_0 \left(\frac{1}{R_{front}} - \frac{1}{R_{back}} \right)$$

Tsujita and al. gives values of cortical tensions ranging from $\approx$ 50 pN/µm for MDA-MB-231 cells to $\approx$ 100 pN/µm for MCF-7 cells[5]. We take an estimate of $\tau_0 \approx 50$ pN/µm for the following calculations. We found that $\Delta P_c \approx 0.05$ mbar at the cell entry and decreases as the cell progresses in the constriction (Fig.S3). Thus we can neglect in the following the pressure difference induced by membrane curvature and consider that cells experience in the constriction a hydrostatic pressure drop of $\Delta P_h \approx 6$ mbar. In fact, ΔP_c represents the minimal pressure required for the cell to enter the constriction. Slowly increasing the pressure to determine the pressure threshold required for the cell to enter the constriction would result in a measure of the cell cortical tension τ_0.

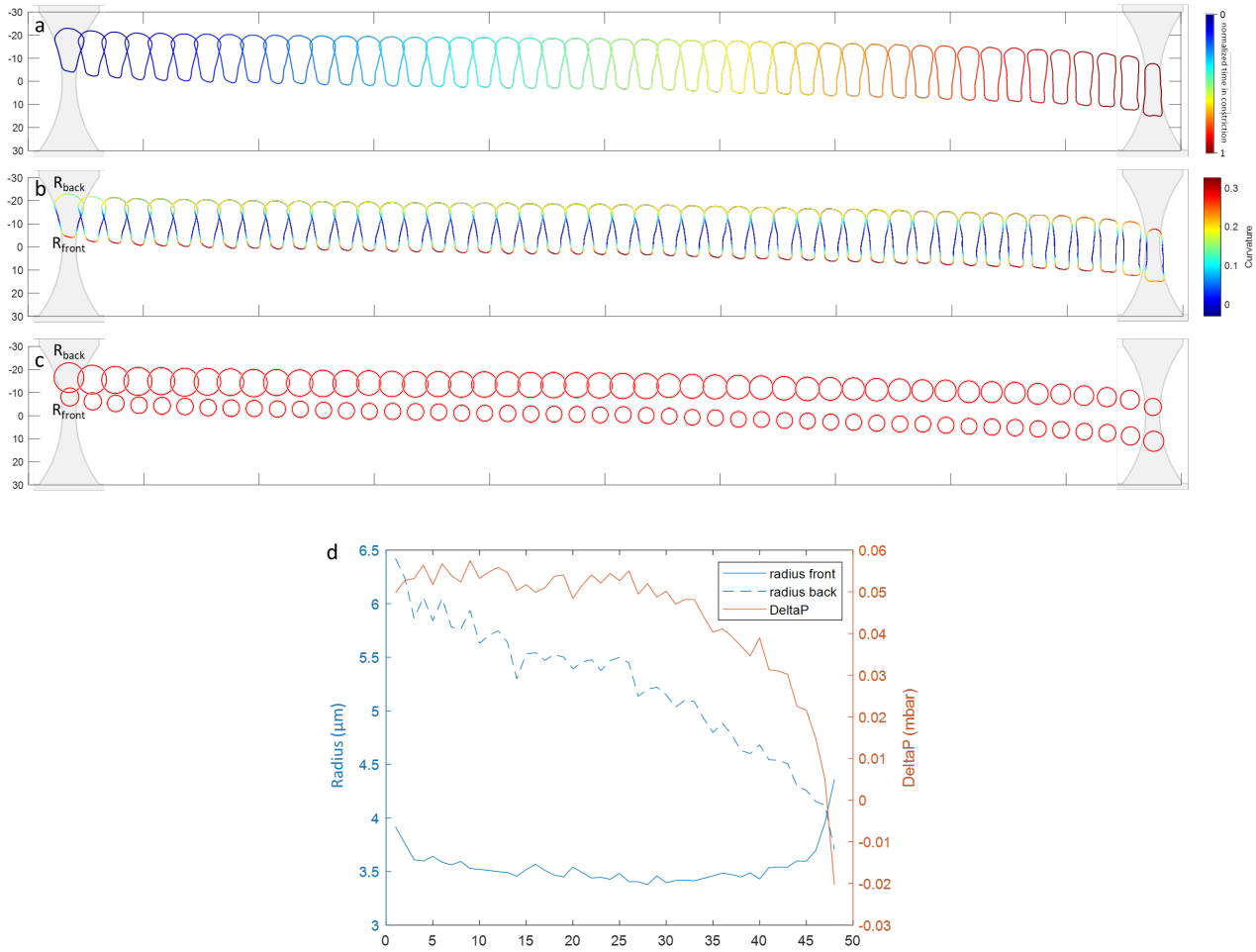

Figure S3 - Evolution of the cell shape as it crosses the constriction and of the pressure difference induced by membrane curvature. a) Outline of the cell presented Fig.2 and Fig.4b as it goes through the constriction. Each image represenetd here is separated by 20ms. b) The radius of curvature was calculated for each point of the cell outline, using the code developed in Driscoll et al.[6]. The color map represents the curvature $C = 1/R$ in μm^{-1}. c) Drawing of the front and back curvature radius. The front (resp. back) of the cell was defined as the 10% of the points with the highest (resp. lowest) y-coordinate in the shape outline. Mean over these points was used to determine front and back radii of the cell. d) Front and back radii were plotted as the cell progresses through the constriction (x-axis is the index of the image of the cell represented above). The resulting pressure difference ΔP_c induced by membrane curvature is represented on the right y-axis.

5 - Cell diameters

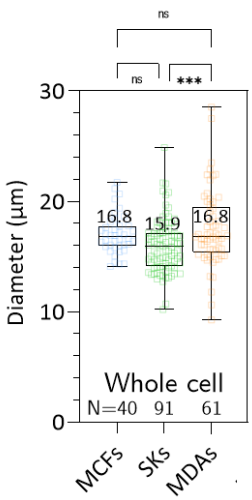

Figure S4 - Cell diameters. The median value is given for each cell line. Interestingly, SK-BR-3 are slightly smaller than the other two cell lines.

6 - Scatter and contour plots

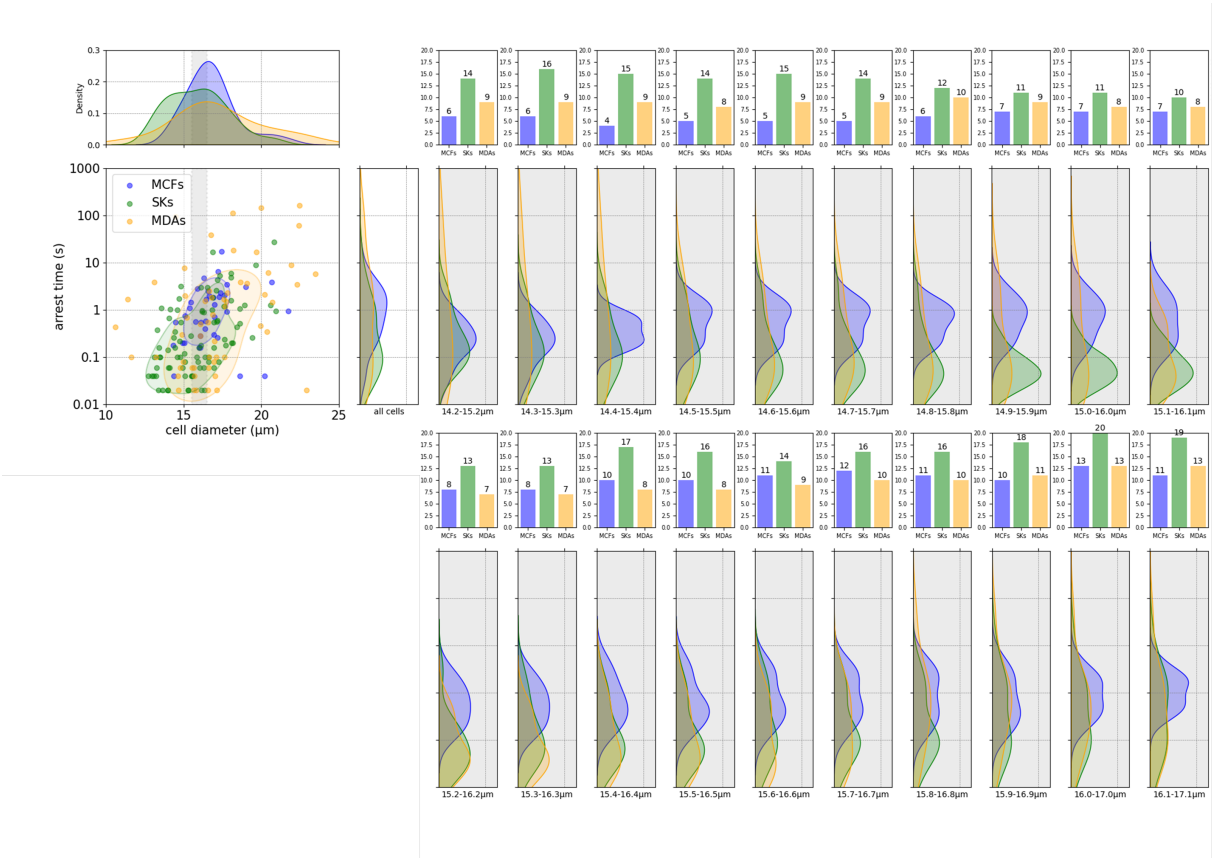

Figure S5 - Scatter plot of arrest time in MCF-7, SK-BR-3 ans MDA-MB-231 cell lines. To compare between cell lines independently of size effects, density plots were sampled on a sliding bin of size 1µm.

7 - Comparison of fits

The normalized deformation data were fit successively with one, two, and three phase decays fits in order to determine the number of exponential decays to be considered. The corresponding fit equations in GraphPad Prism were the following:

- One Phase Decay:
  Y=(Y0 - Plateau)*exp(-X/Tau) + Plateau
- Two Phase Decay:
  SpanFast=(Y0-Plateau)*PercentFast*.01
  SpanSlow=(Y0-Plateau)*(100-PercentFast)*.01
  Y=Plateau + SpanFast*exp(-X/TauFast) + SpanSlow*exp(-X/TauSlow)
- Three Phase Decay:
  YFast=(Y0-Plateau)*PercentFast*.01*exp(-X/TauFast)
  YSlow=(Y0-Plateau)*PercentSlow*.01*exp(-X/TauSlow)
  YMedium=(Y0-Plateau)*(100-PercentFast - PercentSlow)*.01*exp(-X/TauMedium)
  Y=Plateau + YFast + YMedium +YSlow

Alternatively, a power law fit was considered.

- Power Law:
  Y=(X/X0)$\hat{}$(-n)+C

We determined that three phase decay was the best fit to represent the recovery. Addition of more exponential did not increase the quality of the fit, as the software was unable to compute a fourth caracteristic time. From the parameters computed here (Y0, Plateau, PercentFast, TauFast, PercentSlow, TauSlow, PercentMedium, TauMedium), we define as presented in the main text as the following:

- % slow = (PercentSlow)*(Y0-Plateau)
- % medium = (100-PercentFast-PercentSlow)*(Y0-Plateau)
- Φ_{VE} = (% slow + % medium)

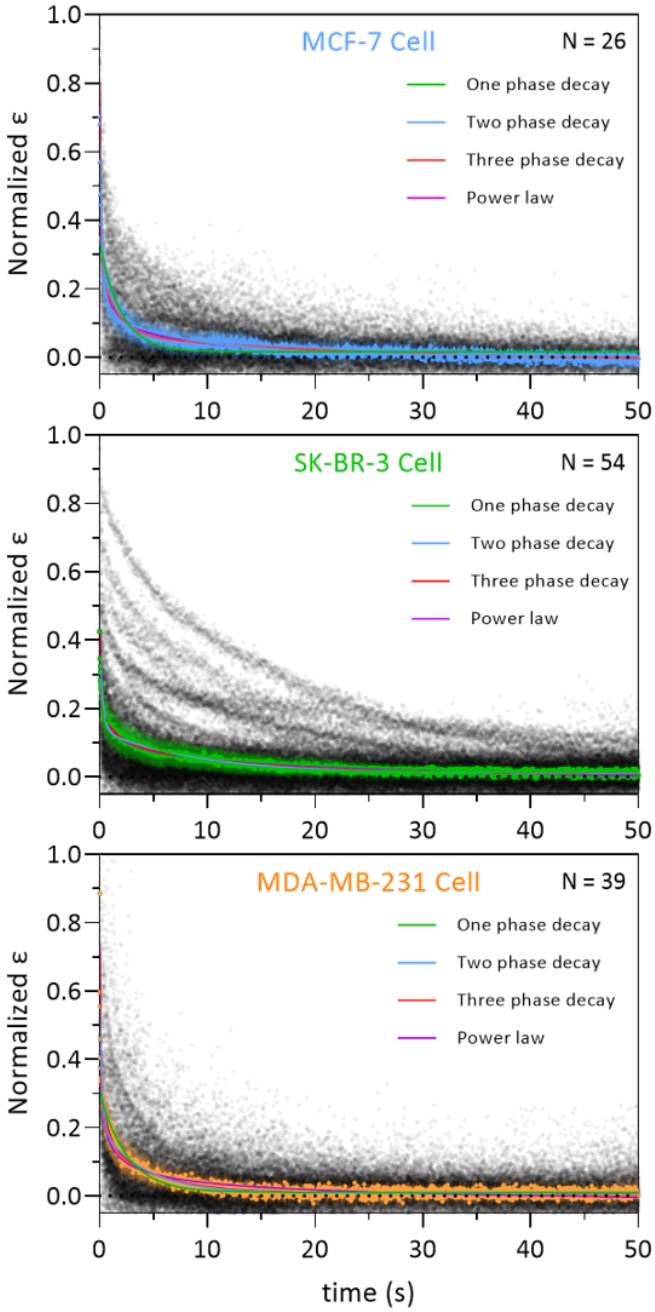

	MCF-7	SK-BR-3	MDA-MB-231
One phase decay			
Best-fit values			
Y0	0,3367	0,18	0,3083
Plateau	0,01616	0,0144	0,01099
Tau	1,963	5,918	2,5
95% CI (profile likelihood)			
Y0	0,3245 to 0,3490	0,1769 to 0,1832	0,3021 to 0,3146
Plateau	0,01516 to 0,01715	0,01371 to 0,01508	0,01030 to 0,01168
Tau	1,834 to 2,103	5,716 to 6,127	2,414 to 2,589
Goodness of Fit			
R squared	0,7983	0,8996	0,8955
Two phase decay			
Best-fit values			
Y0	0,6221	0,3584	0,5462
Plateau	0,003867	0,01054	0,00835
PercentFast	79,93	63,51	63,38
Tau (slow)	8,843	8,731	4,032
Tau (fast)	0,3107	0,3173	0,2452
95% CI (profile likelihood)			
Y0	0,6039 to 0,6408	0,3497 to 0,3674	0,5314 to 0,5617
Plateau	0,002766 to 0,004903	0,01006 to 0,01102	0,007866 to 0,008832
PercentFast	79,31 to 80,53	62,67 to 64,33	62,33 to 64,40
Tau (slow)	8,293 to 9,450	8,511 to 8,961	3,903 to 4,167
Tau (fast)	0,2886 to 0,3348	0,2945 to 0,3418	0,2247 to 0,2674
Goodness of Fit			
R squared	0,94	0,9703	0,9568
Three phase decay			
Best-fit values			
Y0	0,8034	0,4323	0,7154
Plateau	-0,01292	0,008402	0,007731
PercentFast	64,87	52,54	48,01
PercentSlow	10,09	25,08	23,37
Tau (Slow)	23,99	10,84	4,675
Tau (Fast)	0,1105	0,113	0,05563
Tau (Medium)	1,462	1,23	0,5831
95% CI (profile likelihood)			
Y0	0,7849 to 0,8224	0,4201 to 0,4454	0,6796 to 0,7559
Plateau	-0,01660 to -0,009954	0,007839 to 0,008943	0,007254 to 0,008204
PercentFast	63,81 to 65,89	50,82 to 54,15	45,10 to 50,67
PercentSlow	9,779 to 10,42	24,16 to 26,01	21,93 to 24,86
Tau (Slow)	21,51 to 27,12	10,47 to 11,24	4,490 to 4,877
Tau (Fast)	0,1038 to 0,1175	0,1013 to 0,1254	0,04595 to 0,06740
Tau (Medium)	1,376 to 1,553	1,110 to 1,362	0,5140 to 0,6643
Goodness of Fit			
R squared	0,968	0,9771	0,962
Power Law			
Best-fit values			
X0	0,01292	0,0008052	0,01035
n	0,3501	0,18	0,3342
C	-0,05632	-0,1331	-0,06206
95% CI (profile likelihood)			
X0	0,01241 to 0,01343	0,000728 to 0,000888	0,009735 to 0,01097
n	0,3446 to 0,3555	0,1744 to 0,1856	0,3269 to 0,3416
C	-0,05866 to -0,05405	-0,1399 to -0,1268	-0,06540 to -0,05886
Goodness of Fit			
R squared	0,962	0,9713	0,9253

Figure S6 - Fitting of whole cell shape recovery after deformation. For each cell line, the fitting curves obtained with one, two and three phase decays, as well as the fitting curve obtained with the power law were overlayed on the individual cells data points. The parameters obtained for each line are reported in the table on the right. Parameters used in Table 2 are boxed in red.

8 - Treatment of MDA-MB-231 cells with cytoskeletal drugs

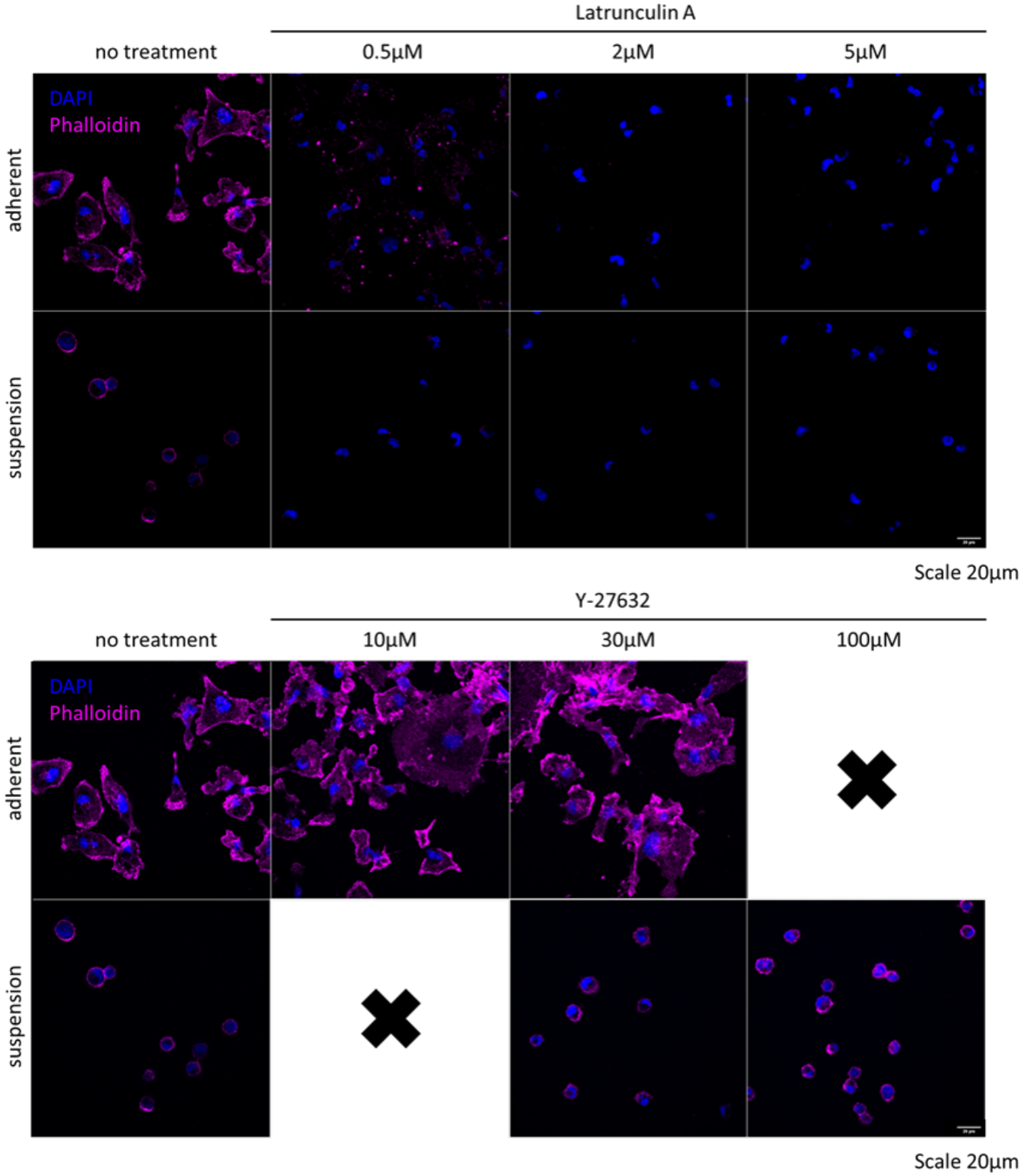

Figure S7 - Treatment of MDA-MB-231 cells with Latrunculin A and Y27632. (top) Treatment with 0.5, 2 and 5µM LatrunculinA. 0.5µM was selected as it induced depolymerisation of the actin cytoskeleton in both adherent and suspension conditions. (bottom) Treatment with 10, 30 and 100µM Y27632. A concentration of 30µM was selected as it increased adherent cells spreading (a proxy for diminution in contractility and thus acto-myosin activity).

9 - Comparison of the recovery dynamics of MDA-MB-231 cells after passing through 6x15 and 9x9 μm^2 constrictions

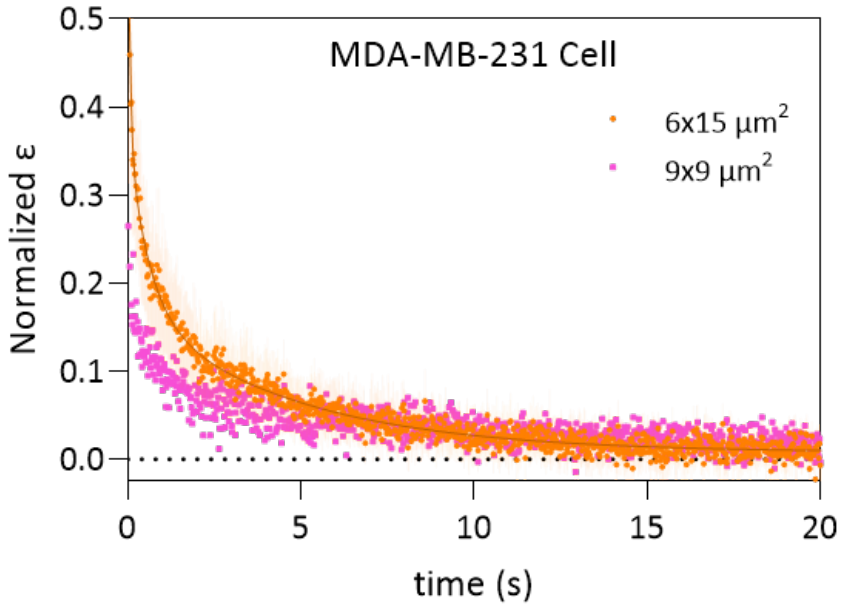

Figure S8 - Recovery of a MDA-MB-231 cell deformed in a square 9x9 μm^2 constriction. Elastic recovery is also present in isotropic square constrictions 9x9 μm^2 of similar section area as 6x15 μm^2 constrictions.

10 - Arrest time of MDA-MB-231 cells submitted to Y-27 and LatA

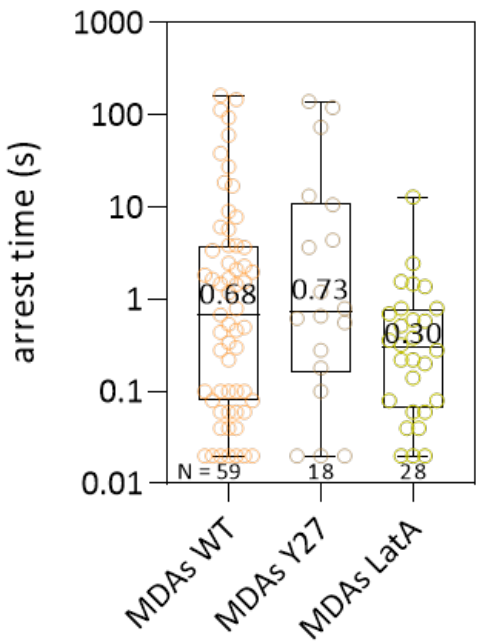

Figure S9 - Box plot of arrest time distribution of WT, Y-27 30 μM and LatA 0.5 μM treated MDA-MB-231 cells. Displayed value represents the median.

11 - Expression levels of p-MLC2 by Western blot

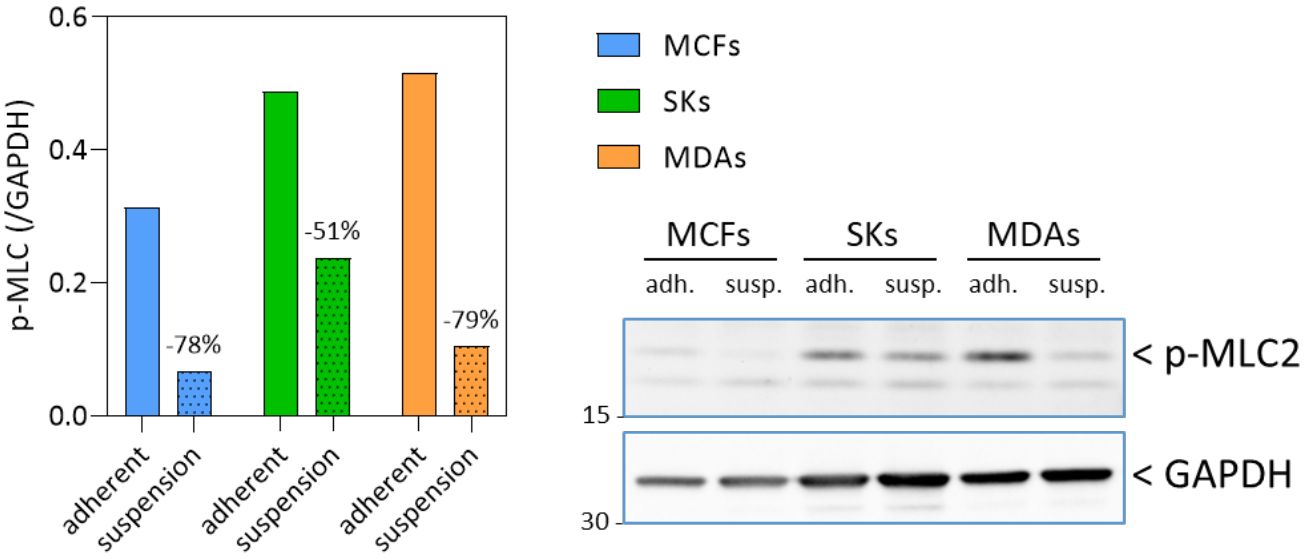

Figure S10 - Western Blots for p-MLC2 (phospho-Myosin Light Chain 2). Adherent (adh.) cells were lysed in the culture dish, while suspended (susp.) cells were lyzed 30min after harvesting.

12-14 - Raw data files

These files correspond to Fig. 3 and Fig.6c (Supp.12, Data Cells.xlsx), Fig. 5 (Supp. 13, Data Deformation.xlsx) and Fig. 6d (Supp. 14, Data Recovery.xlsx).

Notes and references

1 P. M. Davidson, G. R. Fedorchak, S. Mondésert-Deveraux, E. S. Bell, P. Isermann, D. Aubry, R. Allena and J. Lammerding, *Lab on a Chip*, 2019, **19**, 3652–3663.

2 Y. Son, *Polymer*, 2007, **48**, 632–637.

3 E. Evans and A. Yeung, *Biophysical Journal*, 1989, **56**, 151–160.

4 J. Dupire, P. H. Puech, E. Helfer and A. Viallat, *Proceedings of the National Academy of Sciences of the United States of America*, 2020, **117**, 14798–14804.

5 K. Tsujita, R. Satow, S. Asada, Y. Nakamura, L. Arnes, K. Sako, Y. Fujita, K. Fukami and T. Itoh, *Nature Communications*, 2021, **12**, 5930.

6 M. K. Driscoll, C. McCann, R. Kopace, T. Homan, J. T. Fourkas, C. Parent and W. Losert, *PLoS Computational Biology*, 2012, **8**, e1002392.